PHYSICAL REVIEW D **96,** 054511 (2017)

Lattice calculation of coordinate-space vector and axial-vector current correlators in QCD

M. Tomii,[1,*] G. Cossu,[2] B. Fahy,[3] H. Fukaya,[4] S. Hashimoto,[3,5] T. Kaneko,[3,5] and J. Noaki[3]

(JLQCD Collaboration)

[1]*Physics Department, Columbia University, New York 10027, USA*
[2]*School of Physics and Astronomy, University of Edinburgh, Edinburgh EH9 3JZ, United Kingdom*
[3]*Theory Center, Institute of Particle and Nuclear Studies, High Energy Accelerator Research Organization (KEK), Tsukuba 305-0801, Japan*
[4]*Department of Physics, Osaka University, Toyonaka 560-0043, Japan*
[5]*Department of Particle and Nuclear Physics, SOKENAI (Graduate University for Advanced Studies), Tsukuba 305-0801, Japan*

(Received 24 March 2017; published 15 September 2017)

We study the vector and axial-vector current correlators in perturbative and nonperturbative regimes of QCD. The correlators in Euclidean coordinate space are calculated on the lattice using the Möbius domain-wall fermion formulation at three lattice spacings covering 0.044–0.080 fm. The dynamical quark effects of $2+1$ light flavors are included. The sum $V+A$ and the difference $V-A$ of the vector (V) and axial-vector (A) current correlators calculated on the lattice after extrapolating to the physical point agree with those converted from the ALEPH experimental data of hadronic τ decays. The level of the agreement in the $V+A$ channel is about 1.3σ or smaller in the region of $|x| \geq 0.4$ fm, while that in the $V-A$ channel is about 1.8σ at $|x| = 0.74$ fm and smaller at other distances. We also extract the chiral condensate from the short-distance correlators on the lattice using the partially conserved axial current relation. Its result extrapolated to the chiral and continuum limit is compatible with other estimates at low energies.

DOI: 10.1103/PhysRevD.96.054511

I. INTRODUCTION

The two-point current correlator is one of the most fundamental quantities in the study of qantum chromodynamics (QCD). It is defined as a vacuum expectation value of a product of quark currents and reflects the QCD dynamics. It shows different features depending on the distance between the currents. At short distances (< 0.1 fm), it behaves perturbatively, i.e. the perturbative expansion about small coupling constant works reasonably well. Several properties including its scaling are understood perturbatively. In this region, the effect of spontaneous chiral symmetry breaking is small, and two correlators connected by the chiral transformation become almost degenerate. At long distances (> 1 fm), on the other hand, current correlators are saturated by the ground state and are characterized by its mass and decay constant. Degeneracy between the chiral partners is clearly lost.

In the distance region between the two regimes, ~0.1–1 fm, neither the perturbative nor the hadronic description is fully applicable. Terms of higher powers in the QCD coupling constant $\alpha_s(Q)$ become more significant, or the expansion even ceases to converge. This is related to the emergence of power corrections through $e^{1/\beta_0\alpha_s(Q)} \sim (\Lambda_{\mathrm{QCD}}/Q)$ due to the running of the coupling as a function of the scale Q, an inverse of the distance scale. The QCD scale Λ_{QCD} characterizes the distance scale where power corrections of the form $(\Lambda_{\mathrm{QCD}}/Q)^n$ become important. In the hadronic picture, this region is identified by many resonances and multibody scattering states. The individual states involved are complicated, but the common belief is that the sum over a number of hadronic states can be interpreted as interacting quarks and gluons, i.e. quark-hadron duality. There are many sources of evidence that this duality works, such as the perturbative description of the experimentally measured R ratio of the e^+e^- cross section, but theoretical understanding based on QCD is as yet unsatisfactory.

A lattice QCD calculation is, in principle, applicable to any distance scales in Euclidean space. So far, it has been successfully used to calculate hadron correlators at long distances to extract hadron masses and matrix elements, and precise agreement with experimental data for many physical quantities is reported. In such a calculation, the data at the short and middle distances are ignored to avoid "contamination" from excited states, although they may contain interesting information about the intermediate regime where the quark and hadron pictures overlap. In this work, we explore this regime using lattice data.

---

[*] mt3164@columbia.edu

The vector and axial-vector current correlators can be related to hadronic τ decays and e^+e^- hadronic cross section through the optical theorem, which involves a weighted integral over the square of the momentum transfer. This connection between correlators and experimental data allows us to compare the lattice calculation with experiment in the region where excited states contribute significantly.

The vector and axial-vector current correlators in Euclidean space were reconstructed using the early experimental data [1,2]. They provide correlators in coordinate space with spacelike separation x between the currents. This is equivalent to spacelike correlators in momentum space after an appropriate Fourier transform, but allows more direct comparison with the lattice calculation. This sort of comparison was attempted previously using quenched simulations [3–5]. We revisit this problem because there has been considerable progress in lattice calculations and updated experimental data since.

In this work, we study correlators of the isotriplet vector and axial-vector currents. The most recent experimental data for these correlators are obtained through the hadronic τ decay experiment by the ALEPH Collaboration [6]. This experiment provides the spectral functions, which are functions of the invariant mass s, with kinematical upper limits set by the τ lepton mass m_τ^2. Above this limit, the spectral function needs to be estimated using perturbation theory, which is available to the order of α_s^4 [7,8] and reliable at sufficiently large invariant masses. At lower invariant masses, the observed spectral functions show significant deviation from the perturbative prediction due to a violation of quark-hadron duality [9–12]. The duality violation may be modeled using the Regge theory with the large-N_c assumption [11–14].

Our lattice calculation is performed on $2+1$-flavor QCD gauge ensembles. We employ the Möbius domain-wall fermion formulation [15,16] for both sea and valence quarks. Since discretization effects may become more significant at distance scales below 1 fm, we take the continuum limit using ensembles with lattice spacing $a \simeq 0.080$, 0.055 and 0.044 fm. As a result, the correlators at distances larger than $\simeq$0.4 fm are obtained with errors well under control. The same set of gauge ensembles has been used for studying heavy-light decay constants [17], D meson semileptonic form factors [18], the determination of the charm quark mass [19], a calculation of the chiral condensate [20] and the η' mass [21].

We use local vector and axial-vector currents constructed with Möbius domain-wall fermions. Since these currents are not conserving, a finite renormalization is needed. In our previous work [22], we determined the renormalization factor using correlators in the perturbative regime based on the X-space renormalization procedure [23–25]. That is, we determine the renormalization factor such that the lattice correlators at short distances reproduce the continuum perturbative calculation available up to the order of α_s^4 [26] for massless quarks. Since the chiral symmetry on the lattice is precisely maintained, the renormalization factors of the vector and axial-vector currents are identical. The present work is a natural extension of the previous one, as the deviation from the perturbative regime is the main concern.

Besides the comparison with experiment, we extract the chiral condensate from the vector and axial-vector correlators. This appears as the leading power correction to the correlators, reflecting the spontaneous chiral symmetry breaking in QCD. The extraction is based on the partially conserved axial current (PCAC) relation, through which the derivative of the axial-vector correlator is directly related to the chiral condensate [27]. With good control of the discretization effects, we are able to determine the chiral condensate. The result is consistent with another determination from the spectral density of the Dirac operator [20].

This paper is organized as follows. In Sec. II, we discuss the vector and axial-vector current correlators in the continuum theory, including the conversion of the experimental data through a dispersion relation. The relation between the chiral condensate and the axial-vector correlator is also discussed. In Sec. III, we summarize our lattice setup and describe the method to reduce the discretization effect in the lattice correlators. The comparison of the lattice data with experiment and the extraction of the chiral condensate are shown in Sec. IV. Section V concludes the paper with some discussions.

II. CURRENT CORRELATORS

In this work, we study two-point correlation functions of the isotriplet vector and axial-vector currents in Euclidean coordinate space,

$$\Pi_{V,\mu\nu}(x) = \langle V_\mu(x) V_\nu(0)^\dagger \rangle, \quad \Pi_{A,\mu\nu}(x) = \langle A_\mu(x) A_\nu(0)^\dagger \rangle, \tag{1}$$

where the currents are defined by

$$V_\mu(x) = \bar{u}(x)\gamma_\mu d(x), \qquad A_\mu(x) = \bar{u}(x)\gamma_\mu\gamma_5 d(x), \tag{2}$$

with up and down quark fields $u(x)$ and $d(x)$. We also analyze the sum of the Lorentz diagonal components,

$$\Pi_{V/A}(x) = \sum_\mu \Pi_{V/A,\mu\mu}(x). \tag{3}$$

In this work, we take the masses of up and down quarks to be degenerate.

In the momentum space, the corresponding vacuum polarization tensors $\tilde{\Pi}_{V/A,\mu\nu}(Q)$ are given by

$$\begin{aligned}\tilde{\Pi}_{V/A,\mu\nu}(Q) &= \int \mathrm{d}^4 x \mathrm{e}^{-\mathrm{i}Qx}\Pi_{V/A,\mu\nu}(x)\\ &= (Q^2\delta_{\mu\nu} - Q_\mu Q_\nu)\tilde{\Pi}^{(1)}_{V/A}(q^2) - Q_\mu Q_\nu \tilde{\Pi}^{(0)}_{V/A}(q^2),\end{aligned} \tag{4}$$

where $\tilde{\Pi}^{(J)}_{V/A}(q^2)$ is the vacuum polarization function in the spin J channel written as a function of the momentum squared in Minkowski space, $q^2 = -Q^2$.

A. Correlators from experiment

The vector and axial-vector correlators $\Pi_{V/A}(x)$ in coordinate space are related to the experimental observables through a dispersion relation. In the momentum space, it is given by the well-known analyticity formula

$$\tilde{\Pi}^{(J)}_{V/A}(q^2) = \frac{1}{\pi}\int_0^\infty \mathrm{d}s \frac{\mathrm{Im}\tilde{\Pi}^{(J)}_{V/A}(s)}{s-q^2} - \text{subtraction}. \tag{5}$$

Inserting this into (4) and Fourier transforming back to coordinate space, the correlators are found to be [1,2]

$$\Pi_{V/A}(x) = \frac{1}{8\pi^4}\int_0^\infty \mathrm{d}s s^{3/2}(3\rho^{(1)}_{V/A}(s) - \rho^{(0)}_{V/A}(s))\frac{K_1(\sqrt{s}|x|)}{|x|}, \tag{6}$$

where K_1 is the modified Bessel function and $\rho^{(J)}_{V/A}(s) = 2\pi \mathrm{Im}\tilde{\Pi}^{(J)}_{V/A}(s)$ is the *so-called* spectral function. The second term on the rhs of (5), an unphysical contact term, is proportional to $\delta(|x|)$ in coordinate space and is therefore omitted from (6) and in the following discussions.

The spectral function represents the hadronic spectrum associated with the corresponding current and spin J. The spin-1 part $\rho^{(1)}_{V/A}(s)$ is measured by hadronic τ decay experiments [6,28–30]. The spin-0 part of the vector channel vanishes in the isospin limit, while that of the axial-vector channel is dominated by the pion pole, $\rho^{(0)}_A(s) \propto f_\pi^2\delta(s-m_\pi^2)$ with m_π and f_π the pion mass and decay constant, respectively.

Schäfer and Shuryak [2] converted $\rho^{(1)}_{V/A}(s)$ measured by the ALEPH Collaboration [28,29] to the correlators (6), while the contribution of the spin-0 part $\rho^{(0)}_A(s)$ of the axial-vector channel was approximated by using the mass and decay constant of the pion as explained above. Their result was used to test consistency with a quenched lattice simulation [5].

In this work, we use the latest ALEPH data for $\rho^{(1)}_{V/A}(s)$ from τ decays [6] to calculate

$$\Pi^{(1)}_{V/A}(x) = \frac{3}{8\pi^4}\int_0^\infty \mathrm{d}s s^{3/2}\rho^{(1)}_{V/A}(s)\frac{K_1(\sqrt{s}|x|)}{|x|}, \tag{7}$$

which does not contain the contribution of the spin-0 part. In Secs. IV A–IV B, we show the result of the lattice calculation for $\Pi^{(1)}_{V/A}(x)$ extrapolated to the physical point and discuss the consistency with experiment.

Since the spectral functions obtained from hadronic τ decays are measured in a limited region of the invariant mass below the τ lepton mass, $s < m_\tau^2$, we need to complement this using some theory or model for the region $s > m_\tau^2$ in order to estimate the integral in (7). The spectral functions are calculated through order α_s^4 in perturbation theory [7,8], which allows us to precisely estimate the spectral functions in the perturbative regime. Another possibility is to use the operator product expansion (OPE) technique [31], but it is known that the OPE of the spectral functions in the Minkowski domain disagrees with that in full QCD beyond the uncertainty due to the truncation of the perturbative expansion and the operator expansion [9–12]. (Such disagreement is usually referred to as the quark-hadron duality violation.) Due to this, one needs to rely on models to estimate the spectral functions in the region beyond experimental reach. Following a widely used model based on the Regge theory with a large-N_c assumption [11–14], we parametrize the spectral functions at large s as

$$\rho^{(1)}_{V/A}(s) = \rho^{\mathrm{pert}}_{V/A}(s) + \mathrm{e}^{-\delta_{V/A}-\gamma_{V/A}s}\sin(\alpha_{V/A}+\beta_{V/A}s), \tag{8}$$

with the perturbative part $\rho^{\mathrm{pert}}_{V/A}(s)$ of the spectral functions [7,8] and unknown parameters $\delta_{V/A}$, $\gamma_{V/A}$, $\alpha_{V/A}$ and $\beta_{V/A}$. The remnant of resonances appears as the oscillatory term, which is exponentially suppressed at higher energies.

We perform a global fit for the vector and axial-vector spectral functions measured by the ALEPH Collaboration [6] to determine the unknown parameters $\delta_{V/A}$, $\gamma_{V/A}$, $\alpha_{V/A}$ and $\beta_{V/A}$ taking account of the correlation between these two channels. We choose the fit range $1.6\ \mathrm{GeV}^2 \le s \le 2.7\ \mathrm{GeV}^2$, in which the fit function (8) is supposed to be valid and the statistical uncertainty of the experimental data is not too large. As a result of the global fit, we obtain the parameters as

$$\begin{aligned} &\delta_V = 0.32(27), && \gamma_V = 0.72(9)\ \mathrm{GeV}^{-2},\\ &\alpha_V = -2.4(9), && \beta_V = 4.3(2)\ \mathrm{GeV}^{-2},\\ &\delta_A = -1.5(5), && \gamma_A = 1.7(2)\ \mathrm{GeV}^{-2},\\ &\alpha_A = 2.2(4.8), && \beta_A = 3.6(1.2)\ \mathrm{GeV}^{-2}.\end{aligned} \tag{9}$$

There are 24 degrees of freedom and the value of χ^2 per degree of freedom is 1.3.

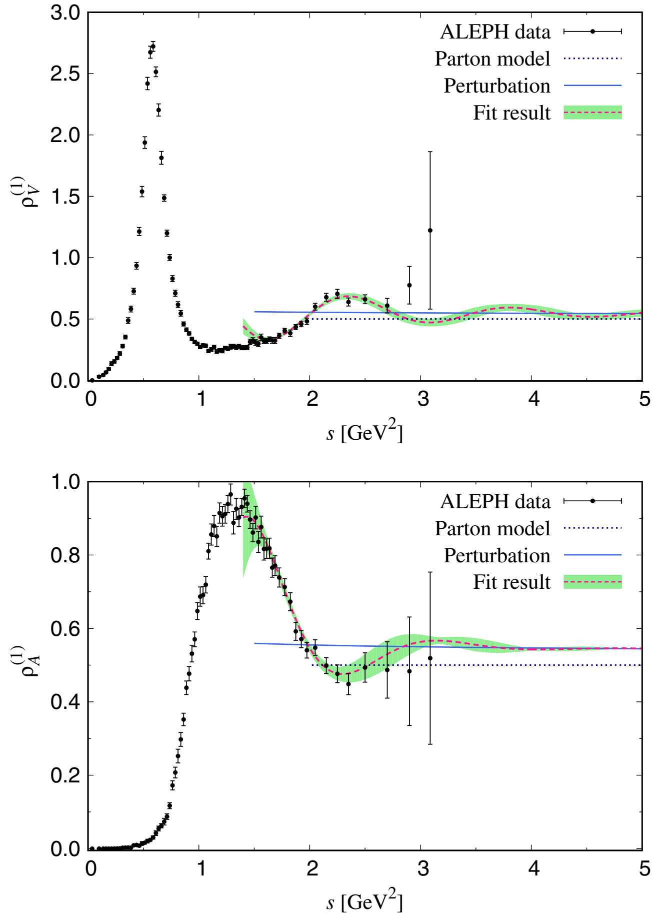

FIG. 1. Spectral functions of the vector (upper) and axial-vector (lower) channels measured by the ALEPH Collaboration (circles) [6] as functions of s. The prediction of the parton model (dotted line), perturbation theory (solid line) and the fit result (dashed curve and band) using the fit function (8) are also shown.

Figure 1 shows the spectral functions in the vector (upper panel) and axial-vector (lower panel) channels measured by the ALEPH Collaboration [6]. The dotted and solid lines stand for the prediction of the parton model (corresponding to the leading order perturbation theory) and the perturbation theory at $O(\alpha_s^4)$, respectively. The fit result is represented by the dashed curve and the band. For the vector channel, the effect of the duality violation is visible as a bump around $s \simeq 2.5$ GeV^2. In order to converge towards the perturbative prediction at high energies, the oscillatory and decaying function of the form $\mathrm{e}^{-\delta_{V/A}-\gamma_{V/A}s}\sin(\alpha_{V/A}+\beta_{V/A}s)$ is necessary.

The correlators reconstructed using (7) are shown in Fig. 2. They are normalized by the tree-level value $R_{V/A}(x)=\Pi_{V/A}^{(1)}(x)/\Pi_0(x)$ with $\Pi_0(x)$ the correlator in the massless free theory, which is the same for the vector and axial-vector channels. We divide the integral (7) into two regions at $s_0 = 2.7$ GeV^2. Below s_0, we directly input the spectral functions from experiment. Above s_0, the spectral functions from massless perturbation theory with (solid band) and without (hatched band) the duality-violating term are used. There are two remaining experimental data points for each channel above s_0 that has been discarded in this analysis due to the large statistical errors. At short distances (< 0.2 fm), these correlators agree with the prediction of massless perturbation theory (dotted line) [26].

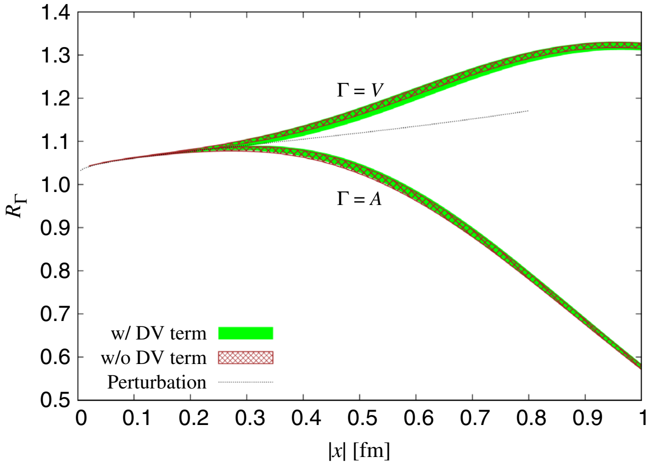

FIG. 2. Vector and axial-vector correlators reproduced using the dispersion relation (7). The spectral functions measured by the ALEPH Collaboration are used for $s \leq 2.7$ GeV^2, while those in $s > 2.7$ GeV^2 are calculated perturbatively with (solid band) and without (hatched band) the duality-violating term. The prediction of the massless perturbation theory is also shown (dotted line).

One can see that the impact of the duality-violating term is not very significant. This is reasonable because the effect of the duality violation is smeared out by the dispersion integral. The vacuum polarization function in the spacelike region is insensitive to the individual poles in the Minkowski domain. We show consistency between these results with the lattice calculation in Secs. IV A–IV B.

It is convenient for later discussions to investigate the size of nonperturbative contributions to the correlators at each distance $|x|$. Figure 3 shows the decomposition of $R_V(x)$ into contributions from the spectral function in different regions of s. The area indicated by "Perturbation" represents the contribution from the spectral function for $s > 2.7$ GeV^2, which is calculated perturbatively. For the more nonperturbative regime, we split the region $s \leq 2.7$ GeV^2 into three: the ρ meson resonance $(0.776-0.150)^2\,\mathrm{GeV}^2 < s < (0.776+0.150)^2\,\mathrm{GeV}^2$, plus the regions above and below it. We also show the corresponding plot for the axial-vector channel in Fig. 4. The region of s indicated by "Perturbation" is the same as for the vector channel, i.e. $s > 2.7$ GeV^2, while the resonance of the a_1 meson is chosen as $(1.23\text{–}0.40)^2$ GeV$^2 < s < (1.23+0.40)^2$ GeV^2. Both plots indicate that the nonperturbative effect is quite significant in the distance region around $|x| \simeq 0.5$ fm,

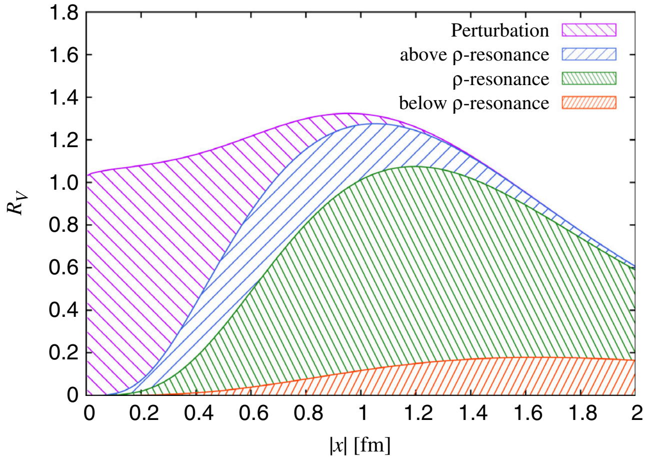

FIG. 3. Decomposition of the vector correlators into contributions from the spectral function in different regions of s.

but the correlators are not saturated by the ground state. This is the region that we are interested in, i.e. neither the perturbative expansion nor low-energy effective theories are fully applicable. In Secs. IV A–IV B, we demonstrate that the lattice calculation succeeds in reproducing the experimental results at $|x| \simeq 0.5$ fm.

B. Chiral condensate through PCAC relation

While the spin-1 part of the vector and axial-vector correlators is related to the hadronic τ decays as discussed in the previous subsection, their spin-0 part is sensitive to another feature of QCD. In the isospin limit, the spin-0 part of the vector channel vanishes, so only the axial-vector channel is nontrivial.

According to the PCAC relation, projection of the axial-vector correlator to the spin-0 part is achieved by taking its divergence. Using the PCAC relation, we can relate the axial-vector correlator to the chiral condensate $\langle \bar{q}q \rangle$ as follows. The spin-0 part of the axial-vector correlator is given by [27,32]

$$\tilde{\Pi}_A^{(0)}(q^2) = \frac{4m_q}{q^4}\langle \bar{q}q \rangle + \frac{4m_q^2}{q^4}\tilde{\Pi}_P(q^2), \qquad (10)$$

where m_q is the degenerate mass of up and down quarks and

$$\tilde{\Pi}_P(q^2) = \int \mathrm{d}^4 x e^{-\mathrm{i}Qx}\langle \bar{u}\mathrm{i}\gamma_5 d(x) \cdot \bar{d}\mathrm{i}\gamma_5 u(0)\rangle. \qquad (11)$$

Therefore, the Fourier transform of (4) leads to

$$-\frac{\pi^2}{2m_q}x^2 \sum_{\mu,\nu} x_\nu \partial_\mu \Pi_{A,\mu\nu}(x) = -\langle \bar{q}q \rangle + O(m_q/x^2). \qquad (12)$$

Here, the renormalization scheme and scale dependence of m_q account for those of $\langle \bar{q}q \rangle$. Taking the chiral limit of (12), we can extract the chiral condensate $\Sigma = -\lim_{m_q \to 0}\langle \bar{q}q \rangle$. While the dependence on mass and $|x|$ is $O(m_q/x^2)$ at short distances, this quantity decreases exponentially at long distances, $\sim e^{-m_\pi |x|}$. This is discussed in Sec. IV C, where we calculate the chiral condensate based on this relation.

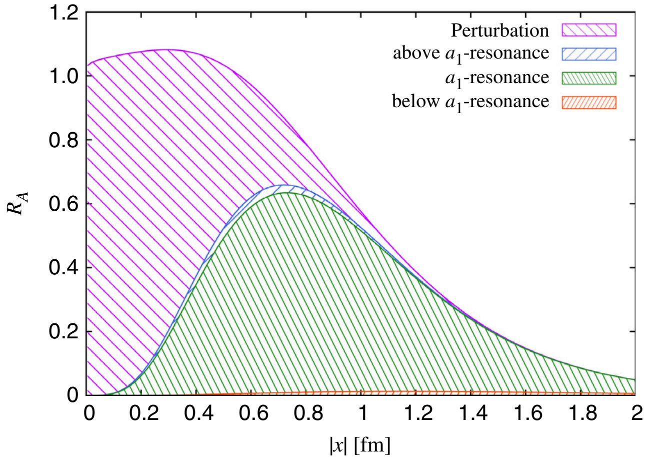

FIG. 4. Same as Fig. 3 but for the axial-vector channel.

III. LATTICE CALCULATION

In this work, we use the lattice ensembles generated with 2 + 1-flavor dynamical Möbius domain-wall fermions [15,16]. The tree-level improved Symanzik action [33] is used for the gauge part and the fermions couple to the gauge links after three steps of the stout smearing [34]. The gauge ensembles used in this analysis are summarized in Table I.

The lattice spacing a ranges between 0.044 and 0.080 fm, with which we take the continuum limit. Their values are determined through the Wilson-flow scale $t_0^{1/2}$ [35] with an input $t_0^{1/2} = 0.1465(21)(13)$ fm taken from [36]. Degenerate up and down quark masses m_q cover a range of pion masses between 230 and 500 MeV. The same masses are used for both sea and valence quarks. The strange quark is, on the other hand, only in the sea, and its mass m_s is taken close to the physical value. The residual mass m_{res} is $O(1)$ MeV on the coarsest lattice and much smaller than that on finer lattices. For each ensemble, $N_{\mathrm{conf}} = 200$ configurations are sampled from 5000 molecular dynamics time. On each configuration, we calculate the correlators with one or more (N_{src}) source points. We use the IroIro + + simulation code [37] for these calculations.

We calculate the current-current correlators $\Pi_{V/A,\mu\nu}(x)$ in (1) with the local vector and axial-vector currents defined on the lattice using Möbius domain-wall fermions. The autocorrelation of correlators exists and is estimated to affect $O(10)$ nearby measurements on the finest lattice, which is examined by varying bin size of jackknife

TABLE I. Lattice ensembles used in this work.

β	a [fm]	$N_s^3 \times N_t \times L_s$	am_s	am_q	am_{res}	aM_π	$N_{\rm conf}$	$N_{\rm src}$
4.17	0.0804	$32^3 \times 64 \times 12$	0.0300	0.0070	0.00017(1)	0.1263(4)	200	4
				0.0120	0.00015(2)	0.1618(3)	200	2
				0.0190	0.00015(3)	0.2030(3)	200	2
		$48^3 \times 96 \times 12$	0.0400	0.0035	0.00022(2)	0.0921(1)	200	2
		$32^3 \times 64 \times 12$		0.0070	0.00023(4)	0.1260(4)	200	4
				0.0120	0.00012(8)	0.1627(3)	200	2
				0.0190	0.00015(3)	0.2033(3)	200	2
4.35	0.0547	$48^3 \times 96 \times 8$	0.0180	0.0042	$\sim 10^{-5}$	0.0820(3)	200	2
				0.0080		0.1127(3)	200	1
				0.0120		0.1381(3)	200	1
			0.0250	0.0042		0.0831(4)	200	2
				0.0080		0.1130(3)	200	1
				0.0120		0.1387(3)	200	1
4.47	0.0439	$64^3 \times 128 \times 8$	0.0150	0.0030		0.0632(2)	200	1

samples. Among 200 configurations analyzed, roughly 20 measurements are statistically independent. The autocorrelation time of the topological charge is about 4 times larger, but we do not find any significant correlation with correlators.

We average correlators that are related by 90° rotations. In this way lattice points of different orientations are distinguished even when they have the same x^2. Namely, the points equivalent to the coordinate (1, 1, 1, 1) are distinct from (2, 0, 0, 0), since they receive different discretization effects.

As discussed in the previous paper [22], we apply some cuts and corrections to reduce the discretization effects. First, we subtract the dominant discretization effect by subtracting the correlators constructed from lattice quarks in the free field theory and add back their continuum counterparts. This procedure is further improved by using the mean-field approximation instead of the free propagator [38]. In addition, we discard the data points that are expected to have large remaining discretization effects. The criterion for the cut is given by an angle θ between the position vector x and the direction (1, 1, 1, 1). Since the lattice data at large θ tend to have large discretization effects [3,25], we neglect the lattice data with $\theta \geq 30°$. This particular value is chosen such that the points with a same x^2 become consistent within the statistical error. More details are described in [22].

IV. RESULTS

A. Consistency of the lattice data with ALEPH in the $V+A$ channel

In this section, we discuss the consistency between the correlators calculated on the lattice and those converted from the ALEPH data for hadronic τ decays. The conversion of the experimental data is discussed in Sec. II A. Here, we analyze the sum and difference of the vector and axial-vector correlators, i.e. the $V+A$ and $V-A$ channels, normalized by the corresponding free correlator $\Pi_0(x)$ in the massless limit

$$R_{V\pm A}(x) = \frac{\Pi_V^{(1)}(x) \pm \Pi_A^{(1)}(x)}{2\Pi_0(x)}. \tag{13}$$

For the lattice calculation, the vector and axial-vector currents need to be renormalized since the local currents we use in this work are not conserving. The renormalization is done multiplicatively, i.e. $R_{V\pm A}(x) \to Z_V^{\overline{\rm MS}}(a)^2 R_{V\pm A}(x)$, with $Z_V^{\overline{\rm MS}}(a)$ the renormalization factor of the vector and axial-vector currents determined in the previous work [22].

Since the quantities $R_{V\pm A}(x)$ do not contain the spin-0 contribution, we also need to subtract the spin-0 part from the lattice correlators to obtain the spin-1 piece $\Pi_{V/A}^{(1)}(x) = \Pi_{V/A}(x) - \Pi_{V/A}^{(0)}(x)$. For the vector channel, the spin-0 part is absent in the isospin limit, $\Pi_V^{(0)}(x) = 0$. For the axial-vector channel, we approximate the spin-0 part $\Pi_A^{(0)}(x)$ by the contribution from the ground state pion. In the infinite volume, it is given by

$$\Pi_A^{(0),\infty}(x) \simeq \frac{z_0 M_\pi^2}{2\pi^2} \frac{K_1(M_\pi |x|)}{|x|}, \tag{14}$$

where z_0 and M_π are extracted from the zero-momentum correlator $\int d^3x \Pi_{A,44}(\vec{x}, t) \to z_0 e^{-M_\pi t}$ at large time separations. We neglect the excited states of the pion because they are not expected to give significant contributions. In a finite box, finite volume effects due to the pion pole may appear. To take account of this, we subtract the wraparound effect of the pion and analyze

$$\Pi_A^{(1)}(x) = \Pi_A(x) - \sum_{x_0} \Pi_A^{(0),\infty}(x - x_0), \tag{15}$$

where the sum over x_0 runs over

$$x_0 \in \{(0,0,0,0), (\pm L,0,0,0), (0,\pm L,0,0), (0,0,\pm L,0), (0,0,0,\pm T), (\pm L,\pm L,0,0), \ldots\}. \tag{16}$$

Figure 5 shows the results for $R_{V+A}(x)$ on the ensembles with $\beta = 4.35$, $am_s = 0.0180$ and with different light quark masses, $am_q = 0.042$, 0.080 and 0.0120. Here, we also show the prediction of massless perturbation theory [26] (dashed line) and the experimental result (band) from the dispersion relation, where the spectral functions $\rho_{V/A}(s)$ in $s > 2.7\ \mathrm{GeV}^2$ include the duality-violating term in (8). In Fig. 5, one can see that the results at smaller masses are closer to the experimental result.

Figure 6 shows the results at pion masses $M_\pi \simeq 300$ MeV but with different β's. We find a significant dependence on the lattice spacing, which can be described by the leading term, which is proportional to a^2 at middle and long distances. As we approach the continuum limit, the lattice data tend to approach the experimental data.

We extrapolate these lattice results to the physical point, i.e. the continuum limit $a \to 0$ and physical pion mass $m_\pi \simeq 140$ MeV. To do so, we first divide the range of $|x|$ into N bins,

$$B_i = [x_i - \delta x/2, x_i + \delta x/2], \quad x_{i+1} = x_i + \delta x, \quad i = 1,2,\ldots,N, \tag{17}$$

where x_i and δx are the center of the ith bin and the width of the bins, respectively. For each bin, we average $R_{V+A}(x)$ over lattice points x in B_i. Since the average depends on the lattice spacing, input mass and the representative distance x_i of the correlator, the average is denoted by $\bar{R}_{V+A}(a, M_\pi, x_i)$ with the explicit dependence on these parameters. Here, we neglect the dependence on the strange quark mass because we do not find significant dependence in the lattice results. We then perform a global fit for all ensembles using the fit function

$$\bar{R}_{V+A}(a, M_\pi, x_i) = R_{V+A}(0, m_\pi, x_i) + c_i(M_\pi^2 - m_\pi^2) + d_i a^2, \tag{18}$$

with three free parameters $R_{V+A}(0, m_\pi, x_i)$, c_i and d_i for each i. The first parameter $R_{V+A}(0, m_\pi, x_i)$ corresponds to the extrapolated value. The other parameters c_i and d_i control the dependences on the pion mass and the lattice spacing, respectively.

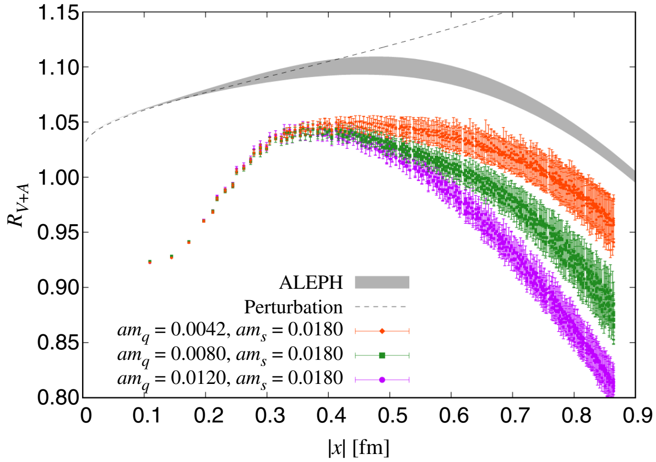

FIG. 5. R_{V+A} calculated on the ensembles with $\beta = 4.35$, $am_s = 0.0180$ and three input light quark masses: $am_q = 0.0042$ (diamonds), 0.080 (squares) and 0.0120 (circles). The prediction of massless perturbation theory (dashed curve) and the results from experiment calculated with the duality-violating term in (8) (band) are also shown.

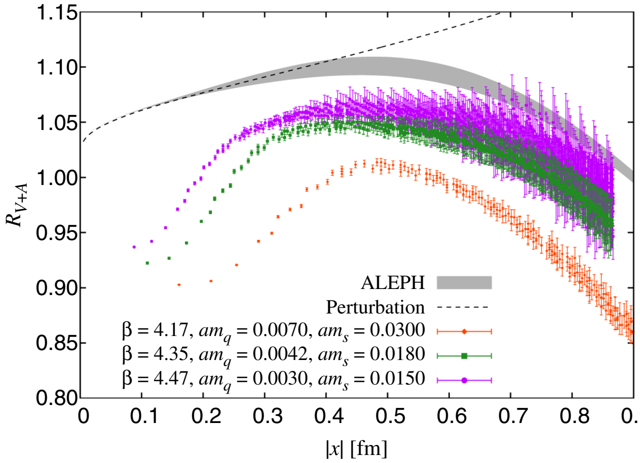

FIG. 6. Same as Fig. 5 but calculated on ensembles with different lattice cutoffs. Pion masses are $M_\pi \simeq 300$ MeV.

Figure 7 shows the result of the extrapolation. Here, we take $\delta x = 0.02$ fm for $x_i \geq 0.4$ fm and $\delta x = 0.04$ fm for $x_i < 0.4$ fm. While the agreement between the lattice result and experiment is found for $|x| > 0.3$ fm in the plot, the fit function (18) may not be appropriate at short distances due to remnant discretization effects that could not be removed by the extrapolation linear in a^2. In order to clarify the appropriate region of the fit function, we show the fit result of the coefficient d_i in Fig. 8 and χ^2/dof in Fig. 9. In Fig. 8, the coefficient d_i varies quite rapidly at $|x| \simeq 0.4$ fm, while it is mostly constant at longer distances. As Fig. 9 shows, χ^2/dof in $|x| < 0.4$ fm is much larger than that in the longer distance regime. These results imply that the remnant discretization effects at $O(a^4)$ are not negligible in $|x| < 0.4$ fm.

To clarify the level of agreement between the lattice calculation and experiment, we analyze the significance of the difference

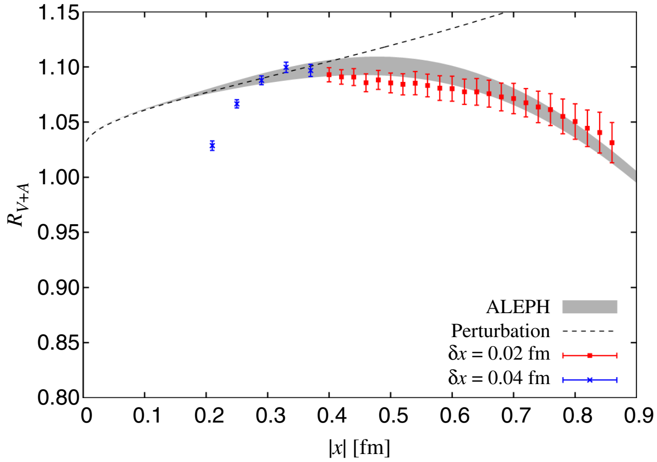

FIG. 7. Lattice result for R_{V+A} after the chiral and continuum extrapolations. Data in each bin are extrapolated assuming (18). The bin size is larger in the short-distance region $|x| \lesssim 0.4$ fm (blue crosses) than others (red squares) as there are fewer lattice points.

$$D_{V\pm A}(x) = \frac{R^{\rm lat}_{V\pm A}(x) - R^{\rm exp}_{V\pm A}(x)}{\sqrt{\delta R^{\rm lat}_{V\pm A}(x)^2 + \delta R^{\rm exp}_{V\pm A}(x)^2}}, \qquad (19)$$

where $R^{\rm lat(exp)}_{V\pm A}(x)$ is the central value of $R_{V\pm A}(x)$ calculated on the lattice (converted from experiment) in Fig. 7 and $\delta R^{\rm lat(exp)}_{V\pm A}(x)$ is its statistical error. Figure 10 shows $D_{V+A}(x)$ and indicates that the lattice calculation agrees with experiment within 1.3σ in the region $|x| \geq 0.4$ fm.

We may conclude that the lattice QCD calculation successfully reproduces the spectral function observed in experiment at length scale of 0.4 fm and larger. The agreement around $|x| \sim 0.5$ fm is important since the precise calculation of the correlators in this region is difficult with perturbative approaches and with low-energy effective theories as discussed in Sec. II A.

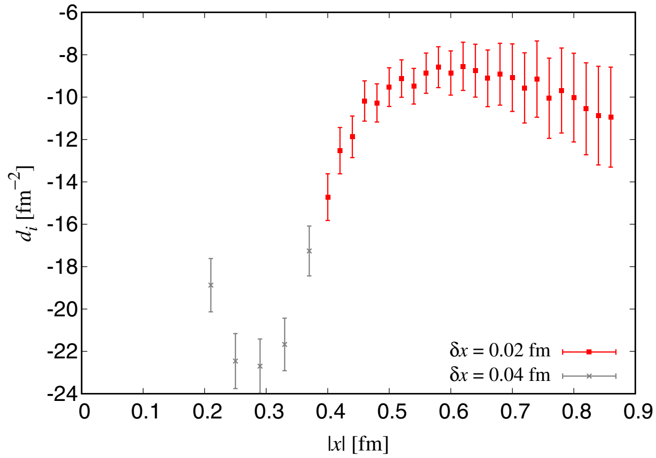

FIG. 8. Fit parameter d_i obtained from the extrapolation of $R_{V+A}(x)$ to the physical point. The result for each bin is plotted as a function of $|x| = x_i$.

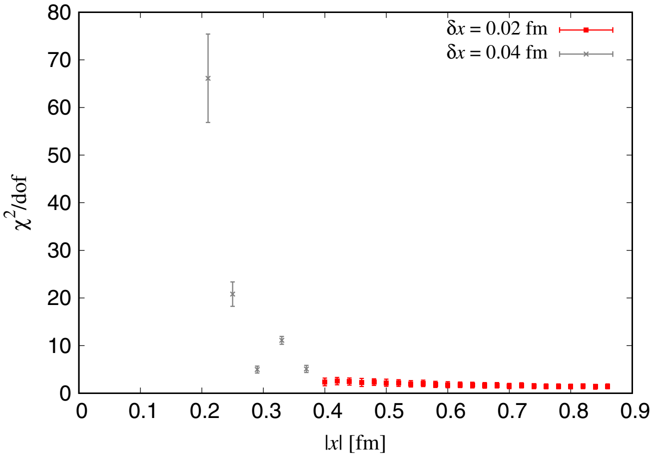

FIG. 9. χ^2 divided by the degrees of freedom for the extrapolation of $R_{V+A}(x)$ to the physical point. The result for each bin is plotted as a function of $|x| = x_i$.

B. Consistency of the lattice data with ALEPH in the $V-A$ channel

Next, we report the results for $R_{V-A}(x)$. Figure 11 shows the lattice data at three different input masses at the same lattice spacing, $\beta = 4.35$. As expected, $R_{V-A}(x)$ vanishes in the short-distance limit because of the good chiral symmetry of the Möbius domain-wall fermion. At short distances ($\lesssim$0.5 fm), the dependence on the input mass is clearly seen and the results at smaller masses are closer to the experimental result.

In Fig. 12, which shows the results at pion masses $M_\pi \simeq$ 300 MeV and at three different β's, there is no significant dependence on the lattice spacing at short distances ($\lesssim$0.5 fm), unlike the case of the $V + A$ channel. One possible reason for this is that the discretization effect on

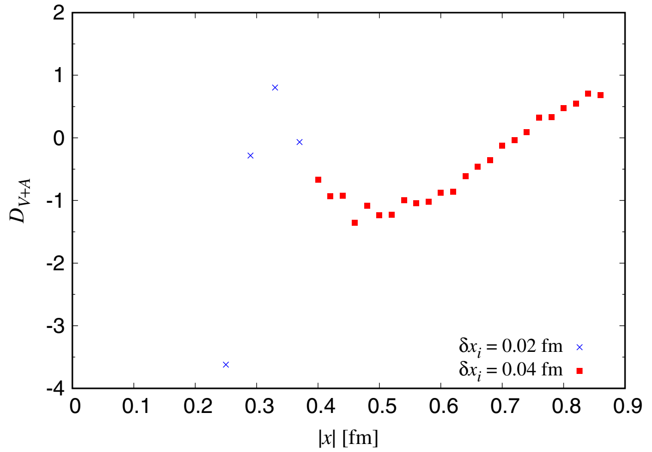

FIG. 10. Significance of the difference $D_{V+A}(x)$ between the lattice calculation and experiment plotted as a function of $|x|$.

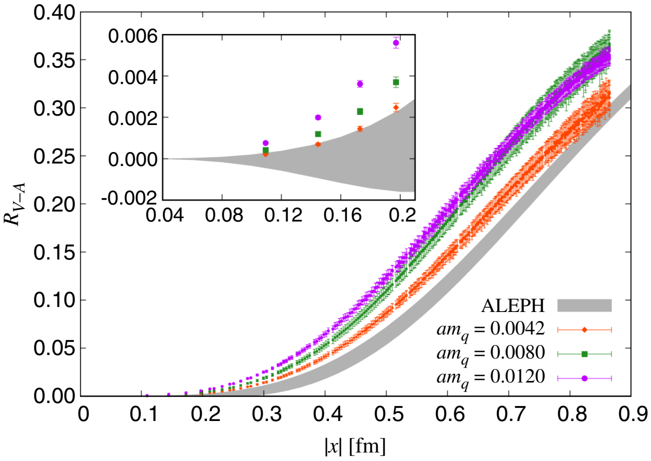

FIG. 11. R_{V-A} calculated on the ensembles with $\beta = 4.35$, $am_s = 0.0180$ and three input light quark masses: $am_q = 0.0042$ (diamonds), 0.080 (squares) and 0.0120 (circles). The results from experiment converted including the duality-violating term in (8) (band) are also shown.

correlators at short distances is mostly perturbative and cancel in the $V - A$ channel.

We extrapolate $R_{V-A}(x)$ to the physical point in the same manner as for the $V + A$ channel. The result is shown in Fig. 13. The consistency between the lattice result and experiment can be seen in the region $|x| > 0.2$ fm. The extrapolation formula works at $|x| \simeq 0.2$ fm as the fit result of d_i and χ^2/dof indicates (Figs. 14 and 15). Unlike the $V + A$ channel, d_i does not vary rapidly and χ^2/dof remains $O(1)$ even at $|x| \simeq 0.2$ fm. At shorter distances there are few lattice points in a bin B_i and the average of $|x|$ over lattice points in the bin could significantly deviate from the center x_i of the bin depending on a. This may lead to another source of a-dependence in $\bar{R}_{V-A}(a, M_\pi, x_i)$, which may not be taken into account by our fit procedure. Although we do not extrapolate the lattice data in $|x| < 0.2$ fm for this reason, Figs. 11 and 12 indicate that the lattice data agree with the phenomenological curve even in the asymptotically small $|x|$ region. Figure 16 shows the significance of the difference $D_{V-A}(x)$ between the lattice calculation and experiment. The largest difference, $\sim 1.8\sigma$, is seen at $|x| = 0.74$ fm, while 1σ agreement is seen below 0.5 fm, except for at $|x| = 0.33$ fm, where the fit function may not be appropriate as explained above.

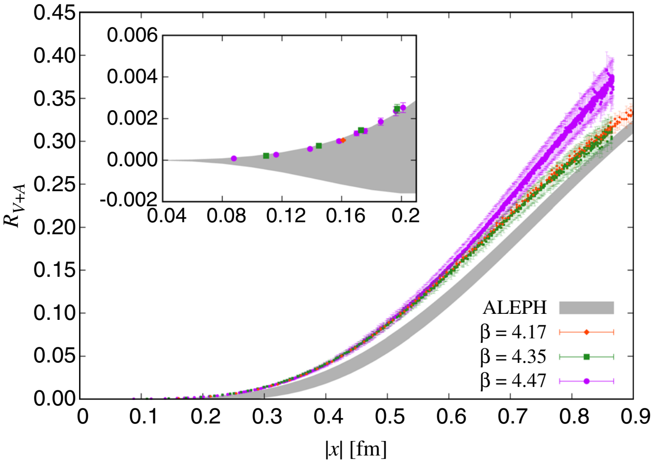

FIG. 12. Same as Fig. 11 but calculated on ensembles with different lattice cutoffs. Pion masses are $M_\pi \simeq 300$ MeV.

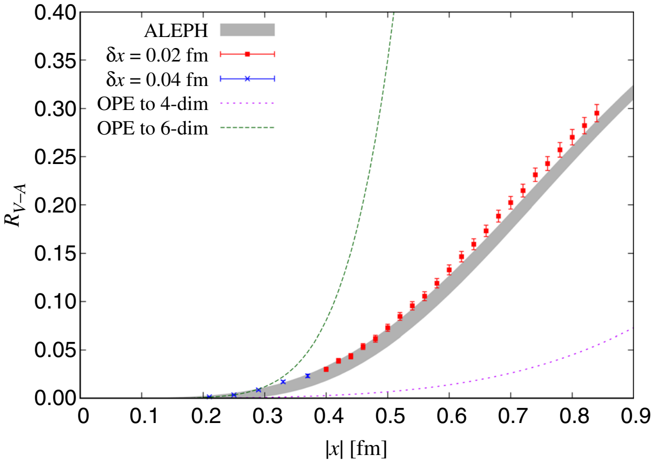

FIG. 13. Lattice result for R_{V-A} after the chiral and continuum extrapolations. Data in each bin are extrapolated assuming (18). The bin size is larger in the short-distance region $|x| \lesssim 0.4$ fm (blue crosses) than others (red squares) as there are fewer lattice points. The experimental result (band) and the predictions of the OPE including up to dimension-4 (dotted curve) and dimension-6 (dashed curve) operators are also plotted.

Figure 13 also shows the predictions of the OPE including up to dimension-4 (dotted curve) and dimension-6 (dashed curve) operators. The OPE $R^{\mathrm{OPE}}_{V-A}(x)$ of the $V - A$ channel is written as

$$R^{\mathrm{OPE}}_{V-A}(x) = -\frac{\pi^2}{3} m_q \langle \bar{q} q \rangle x^4 + \frac{\alpha_s \pi^3}{9} \langle \bar{q} q \rangle^2 \ln(\mu_0 x)^2 x^6 - \frac{f_\pi^2 m_\pi^3 \pi^2}{48} |x|^5 K_1(m_\pi |x|) + O(m_q^2). \tag{20}$$

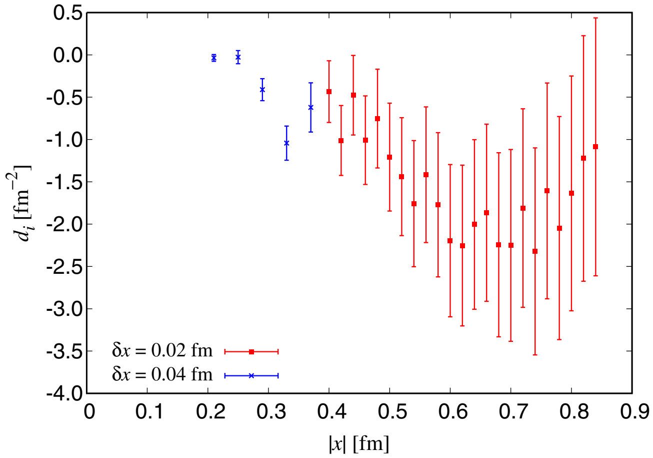

FIG. 14. Same as Fig. 8 but for the $V - A$ channel.

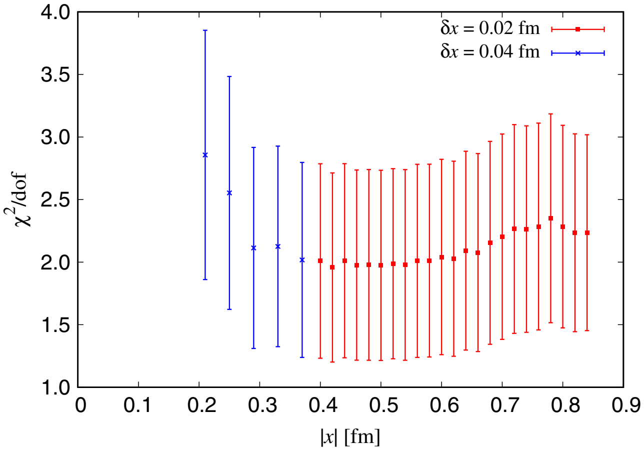

FIG. 15. Same as Fig. 9 but for the $V-A$ channel.

Here, only the leading order of the strong coupling constant α_s is shown for the first and second terms. The first term is calculated by the Fourier transform of the OPE in the momentum space given in [31]. The second term is estimated using the vacuum saturation approximation with $\langle\bar{q}q\rangle^2$ [39]. Before the normalization of (13), this term is logarithmic in x with an unknown parameter μ_0 as a result of the Fourier transform $Q^{-4} \to -\frac{1}{16\pi^2}\ln(\mu_0 x)^2$. Since the first two terms on the right-hand side of (20) correspond to the OPE including the longitudinal component of the axial-vector correlators, we subtract the contribution of the pion pole by the third term. In the evaluation of $R^{\mathrm{OPE}}_{V-A}(x)$ shown in Fig. 13, we set nominal values $f_\pi = 130$ MeV, $m_\pi = 140$ MeV, and the scheme-dependent parameters at 2 GeV in the $\overline{\mathrm{MS}}$ scheme, $\alpha_s = 0.3$, $m_q = 3.4$ MeV, $\langle\bar{q}q\rangle = -(270\ \mathrm{MeV})^3$. We also set $\mu_0 = 2$ GeV as a typical value. The result of the truncation at dimension-4 already deviates from the lattice result at 0.3 fm. Including the dimension-6 operators, it still disagrees with the lattice result in the region $|x| > 0.3$ fm.

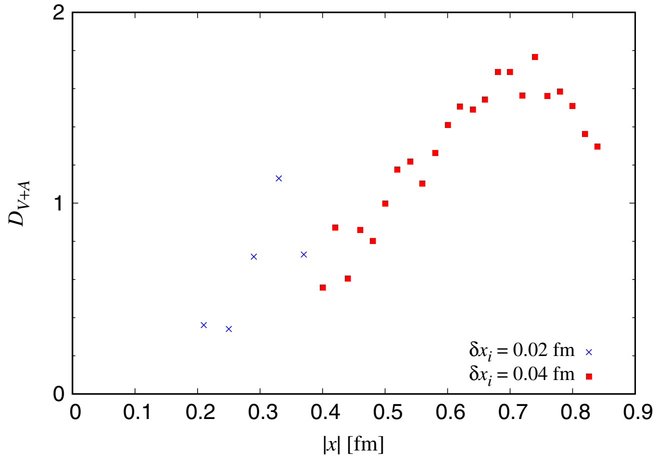

FIG. 16. Significance of the difference $D_{V-A}(x)$ between the lattice calculation and experiment plotted as a function of $|x|$.

This analysis demonstrates the limitation of the operator expansion quantitatively. The distance scale where the OPE can be safely used depends on the channel. In the $V-A$ channel, it can only be safely used at $\lesssim 0.3$ fm.

C. Chiral condensate

Here, we show our analysis to extract the chiral condensate through the PCAC relation. The basic recipe, which is valid in the continuum theory, is explained in Sec. II B.

On the lattice, some modifications to (12) are needed. The violation of the current conservation induces substantial discretization effects from the derivative term. Such discretization effects can be largely eliminated by subtracting the vector counterpart, which vanishes in the continuum theory.

We analyze

$$\Sigma^{V/A}_{m_q}(x) = -\frac{\pi^2}{2(m_q+m_{res})}x^2\sum_{\mu,\nu}x_\nu\nabla_\mu\Pi^\infty_{V/A,\mu\nu}(x), \qquad (21)$$

where the derivative ∇_μ on the lattice is defined as

$$\nabla_\mu f(x) = \frac{f(x+a\hat{\mu}) - f(x-a\hat{\mu})}{2a}, \qquad (22)$$

with $\hat{\mu}$ being the unit vector along the μ-direction. The residual mass m_{res} is added to the quark mass to take account of the violation of the Ginsparg-Wilson relation due to finite L_s.

In (21), we use the correlators $\Pi^\infty_{V/A,\mu\nu}(x)$ after subtracting the finite volume effect. Here, we assume that there is no significant finite volume effect for the vector channel, $\Pi^\infty_{V,\mu\nu}(x) = \Pi_{V,\mu\nu}(x)$, which is justified because the single pion does not propagate in this channel. The finite volume effect on the axial-vector channel is estimated as the wraparound effect of the pion as in the previous section. The asymptotic form of $\sum_{\mu,\nu}x_\nu\nabla_\mu\Pi^\infty_{A,\mu\nu}(x)$ at long distances is given by

$$\sum_{\mu,\nu}x_\nu\nabla_\mu\Pi^\infty_{A,\mu\nu}(x) \to \frac{M_\pi^2 z_0}{2\pi^2}\sum_\mu x_\mu\partial_\mu\frac{K_1(M_\pi|x|)}{|x|}, \qquad (23)$$

where z_0 and M_π may be extracted from the zero-momentum correlator, $\int d^3x\Pi_{A,44}(\vec{x},t) \to z_0 e^{-M_\pi t}$. We can thus subtract the finite volume effect from the lattice data by

$$\sum_{\mu,\nu}x_\nu\nabla_\mu\Pi^\infty_{A,\mu\nu}(x) = \sum_{\mu,\nu}x_\nu\nabla_\mu\Pi_{A,\mu\nu}(x) - \frac{M_\pi^2 z_0}{2\pi^2}\sum_{\mu,x_0}x_\mu\partial_\mu\frac{K_1(M_\pi|x-x_0|)}{|x-x_0|}, \qquad (24)$$

where the sum over x_0 runs over

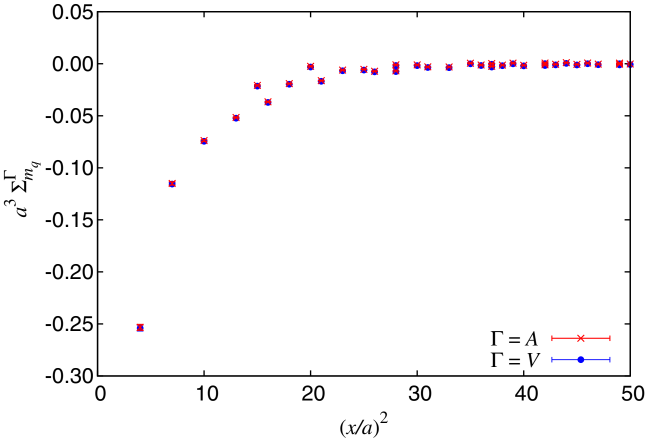

FIG. 17. $\Sigma^{V/A}_{m_q}$ as functions of $(x/a)^2$ calculated on the ensemble with $\beta = 4.35$ and $(am_q, am_s) = (0.0042, 0.0180)$.

$$x_0 \in \{(\pm L, 0, 0, 0), (0, \pm L, 0, 0), (0, 0, \pm L, 0), (0, 0, 0, \pm T), (\pm L, \pm L, 0, 0), \ldots\}. \tag{25}$$

Figure 17 shows the lattice result for $\Sigma^{V/A}_{m_q}(x)$ calculated on one of the ensembles. In the continuum theory, the axial-vector channel $\Sigma^{A}_{m_q}(x)$ is equal to the chiral condensate up to the correction of $O(m_q)$, as shown in (12), and the vector channel is identically zero. Figure 17 indicates that the axial-vector channel calculated on the lattice almost coincides with the vector channel and is nonzero, because of the nonconserving (axial-)vector currents. In other words, the axial-vector channel is largely contaminated by discretization effects, by the same amount as in the vector channel. The precise chiral symmetry realized by Möbius domain-wall fermion is the source of this coincidence.

Therefore, we may cancel the bulk of the discretization effects by analyzing

$$\Sigma_{m_q}(x) = \Sigma^{A}_{m_q}(x) - \Sigma^{V}_{m_q}(x), \tag{26}$$

which reduces to $\Sigma^{A}_{m_q}(x)$ in the continuum theory. Figure 18 shows the cubic root of $\Sigma_{m_q}(x)$ calculated at three different masses and the same β. The renormalization is done multiplicatively to the $\overline{\mathrm{MS}}$ scheme at 2 GeV,

$$\Sigma^{\overline{\mathrm{MS}}}_{m_q}(2\ \mathrm{GeV}; x) = Z^{\overline{\mathrm{MS}}}_{V}(a)^2 Z^{\overline{\mathrm{MS}}}_{S}(2\ \mathrm{GeV}; a)\Sigma_{m_q}(x) \tag{27}$$

with the renormalization factors $Z^{\overline{\mathrm{MS}}}_{V}(a)$ and $Z^{\overline{\mathrm{MS}}}_{S}(2\ \mathrm{GeV}; a)$ determined in the previous work [22]. The gray band represents the FLAG average [40] of the chiral condensate $(\Sigma^{\overline{\mathrm{MS}}}(2\ \mathrm{GeV}))^{1/3} = 274 \pm 3$ MeV at $n_f = 2 + 1$.

In Fig. 18, the results at smaller masses are closer to the FLAG average. This agrees with the theoretical expectation discussed in Sec. II B that the chiral condensate

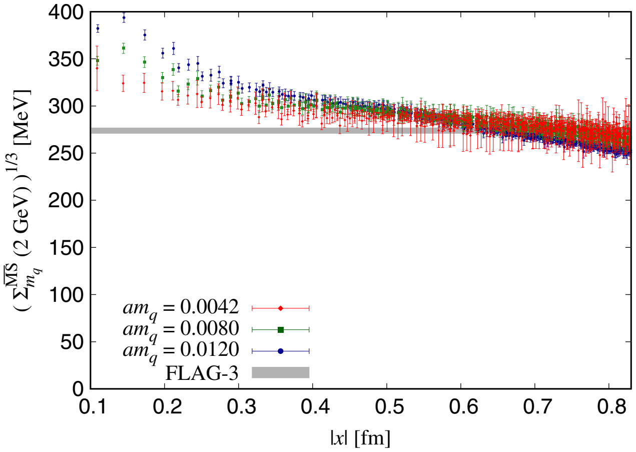

FIG. 18. $(\Sigma^{\overline{\mathrm{MS}}}_{m_q}(2\ \mathrm{GeV}))^{1/3}$ calculated on the ensembles with $\beta = 4.35$, $am_s = 0.0180$ and at three input light quark masses: $am_q = 0.0042$ (diamonds), 0.080 (squares) and 0.0120 (circles). The gray band shows the FLAG average $(\Sigma^{\overline{\mathrm{MS}}}(2\ \mathrm{GeV}))^{1/3} = 274(3)$ MeV.

$\Sigma^{\overline{\mathrm{MS}}}(2\ \mathrm{GeV})$ is obtained in the chiral limit of $\Sigma^{\overline{\mathrm{MS}}}_{m_q}(2\ \mathrm{GeV}; x)$. Figure 19 shows the results at three different lattice spacings with pion masses $M_\pi \simeq 300$ MeV. Like for $R_{V-A}(x)$, there is no significant dependence on the lattice spacing.

We extrapolate these results to the chiral and the continuum limits as follows. The average $\bar{\Sigma}^{\overline{\mathrm{MS}}}_{m_q}(2\ \mathrm{GeV}; a, M_\pi, x_i)$ of $\Sigma^{\overline{\mathrm{MS}}}_{m_q}(2\ \mathrm{GeV}; x)$ over lattice points in each bin is defined similarly to $\bar{R}_{V\pm A}(a, M_\pi, x_i)$ in the previous subsections. Unlike for $R_{V\pm A}(x)$, the x-dependence of $\Sigma_{m_q}(x)$ is limited to $O(M_\pi^2)$ or $O(a^2)$, and the result of the extrapolation of $\Sigma_{m_q}(x)$ must be independent of x. We therefore perform a simultaneous fit for all bins using the fit function

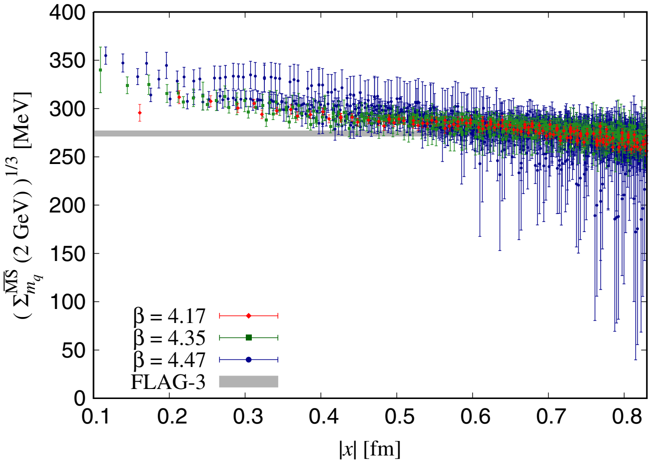

FIG. 19. Same as Fig. 18 but calculated on ensembles with different lattice cutoffs and pion masses are $M_\pi \simeq 300$ MeV.

TABLE II. Chiral condensate extracted from the global fit using (28) at various fit ranges and bin widths.

$x_1 - \delta x/2$ [fm]	$x_N + \delta x/2$ [fm]	δx [fm]	N	$\Sigma^{\overline{\mathrm{MS}}}(2\ \mathrm{GeV})^{1/3}$ [MeV]
0.23	0.83	0.02	30	284.3(4.0)
0.23	0.83	0.04	15	285.2(4.0)
0.23	0.83	0.06	10	284.5(4.0)
0.23	0.83	0.10	6	285.7(4.0)
0.23	0.43	0.04	5	293.7(5.4)
0.31	0.51	0.04	5	290.7(5.0)
0.39	0.59	0.04	5	288.9(4.6)
0.47	0.67	0.04	5	285.5(4.4)
0.55	0.75	0.04	5	280.8(4.0)
0.63	0.83	0.04	5	276.2(3.8)

$$\left(\bar{\Sigma}^{\overline{\mathrm{MS}}}_{m_q}(2\ \mathrm{GeV}; a, M_\pi, x_i)\right)^{1/3} = \left(\Sigma^{\overline{\mathrm{MS}}}(2\ \mathrm{GeV})\right)^{1/3} + c_i M_\pi^2 + d_i a^2, \quad i = 1, 2, \ldots, N, \tag{28}$$

with $2N+1$ parameters $c_1, c_2, \ldots, c_N, d_1, d_2, \ldots, d_N$ and $(\Sigma^{\overline{\mathrm{MS}}}(2\ \mathrm{GeV}))^{1/3}$.

At short distances, the continuum extrapolation may be contaminated because there are few data points in each bin. At long distances, on the other hand, the extrapolation by the fit function (28) may not be appropriate since the mass dependence of $\Sigma_{m_q}(x)$ may be complicated, as described in (23). We extrapolate lattice data at middle distances where the dependences on the pion mass and lattice spacing would be well under control by the fit function (28).

Table II summarizes the results at several fit ranges and widths of bins. The dependence on δx is sufficiently small compared to the statistical error. On the other hand, the dependence on the fit range is larger than the statistical error. Including this uncertainty in the estimate of the systematic error, we determine the chiral condensate to be

$$\left(\Sigma^{\overline{\mathrm{MS}}}(2\ \mathrm{GeV})\right)^{1/3} = 284.9 \pm 4.0_{\mathrm{stat}} \pm 8.8_{\mathrm{sys}}\ \mathrm{MeV}. \tag{29}$$

Here, the central value and the statistical error are estimated by an average of the four results for the fit range 0.23–0.83 fm with various widths δx, while the systematic error is estimated as the maximum difference between the central value and the results at various fit ranges. This result agrees well with the result obtained from the Dirac spectrum on the same set of lattice ensembles, 270.0(4.9) MeV [20].

V. CONCLUSION

We have discussed the vector and axial-vector current correlators in the distances between the perturbative and nonperturbative regimes. In this intermediate region, neither the perturbative approaches nor low-energy effective theories are fully applicable. Lattice calculation can be used to analyze such theoretically difficult physical regions, provided that the systematic errors are properly estimated. The τ decay experiment by the ALEPH Collaboration played a crucial role as it provides the data for both the vector and axial-vector channels. The $V+A$ channel is mainly useful to test the perturbation theory, while the $V-A$ is sensitive to the nonperturbative aspects of QCD. The lattice calculation of the $V+A$ channel agrees with experiment in the length scale of $|x| \geq 0.4$ fm at the level of 1.3σ or better. The $V-A$ channel agrees at a level of 1.8σ at $|x| = 0.74$ fm or even better agreement at other distances. The chiral condensate, the order parameter of chiral symmetry breaking, is also precisely extracted from this analysis.

The consistency between the lattice calculation and the experimental data seen in this work adds further support for the validity of QCD in the distance region where excited states contribute significantly. The lattice calculation of the current correlators can also identify the region where the correlators are well explained by the OPE, which is the main theoretical tool in phenomenological analyses.

The method applied in this work to extract the chiral condensate needs a differential of the axial-vector correlator on the lattice. The substantial discretization error from the differential is dramatically reduced by subtracting the counterpart of the vector channel. The fact that the obtained chiral condensate agrees with the result based on the Banks-Casher relation gives additional confidence in our description of the symmetry broken QCD vacuum.

Lattice calculations of current correlators at finer lattices, which will become available in the near future, would be very interesting as they may give further information in the perturbative regime. They will provide us with stringent tests of the perturbative expansion in QCD, which is now available to $O(\alpha_s^4)$ for the vacuum polarization function. At the same time, they would be a sensitive probe to determine the strong coupling constant.

While this work focused on the vector and axial-vector channels, the scalar and pseudoscalar correlators may reflect a different aspect of QCD. The perturbative region for these correlators is much shorter than that of the vector and axial-vector channels because they are directly affected by instanton interactions [41]. Lattice calculations of the scalar and pseudoscalar correlators may give new insights into understanding such effects.

ACKNOWLEDGMENTS

Numerical simulations are performed on the Hitachi SR16000 and IBM Blue Gene/Q at KEK under a support of its Large Scale Simulation Program

(Programs No. 15/16-09, No. 16/17-14). We thank P. Boyle for providing the highly optimized code for Blue Gene/Q. We also thank B. Colquhoun for careful reading of the manuscript. This work is supported in part by the US DOE grant (Grant No. DE-SC0011941), the Grant-in-Aid of the Japanese Ministry of Education (Grants No. 25800147, No. 26247043, No. 26400259) and the Post-K supercomputer project through JICFuS.

---

[1] E. V. Shuryak, Rev. Mod. Phys. **65**, 1 (1993).
[2] T. Schaefer and E. V. Shuryak, Phys. Rev. Lett. **86**, 3973 (2001).
[3] M. C. Chu, J. M. Grandy, S. Huang, and J. W. Negele, Phys. Rev. D **48**, 3340 (1993).
[4] S. J. Hands, P. W. Stephenson, and A. McKerrell (UKQCD Collaboration), Phys. Rev. D **51**, 6394 (1995).
[5] T. A. DeGrand, Phys. Rev. D **64**, 094508 (2001).
[6] M. Davier, A. Hocker, B. Malaescu, C.-Z. Yuan, and Z. Zhang, Eur. Phys. J. C **74**, 2803 (2014).
[7] P. A. Baikov, K. G. Chetyrkin, and J. H. Kuhn, Phys. Rev. Lett. **101**, 012002 (2008).
[8] P. A. Baikov, K. G. Chetyrkin, and J. H. Kuhn, Nucl. Phys. B, Proc. Suppl. **189**, 49 (2009).
[9] M. A. Shifman, in Minneapolis 1994, Continuous advances in QCD 1994, p. 249.
[10] B. Blok, M. A. Shifman, and D.-X. Zhang, Phys. Rev. D **57**, 2691 (1998); **59**, 019901 (1998).
[11] *At the Frontier of Particle Physics*, edited by M. A. Shifman (World Scientific, Singapore, 2001), Vol. 3, p. 1447.
[12] I. I. Y. Bigi and N. Uraltsev, Int. J. Mod. Phys. A **16**, 5201 (2001).
[13] O. Cata, M. Golterman, and S. Peris, Phys. Rev. D **79**, 053002 (2009).
[14] D. Boito, M. Golterman, M. Jamin, A. Mahdavi, K. Maltman, J. Osborne, and S. Peris, Phys. Rev. D **85**, 093015 (2012).
[15] R. C. Brower, H. Neff, and K. Orginos, Nucl. Phys. B, Proc. Suppl. **140**, 686 (2005).
[16] R. C. Brower, H. Neff, and K. Orginos, arXiv:1206.5214.
[17] B. Fahy, G. Cossu, S. Hashimoto, T. Kaneko, J. Noaki, and M. Tomii, *Proc. Sci.*, LATTICE2015 (2016) 074.
[18] T. Kaneko, B. Fahy, H. Fukaya, and S. Hashimoto (JLQCD Collaboration), *Proc. Sci.*, LATTICE2016 (2017) 297.
[19] K. Nakayama, B. Fahy, and S. Hashimoto, Phys. Rev. D **94**, 054507 (2016).
[20] G. Cossu, H. Fukaya, S. Hashimoto, T. Kaneko, and J.-I. Noaki, Prog. Theor. Exp. Phys. **2016**, 093B06 (2016).
[21] H. Fukaya, S. Aoki, G. Cossu, S. Hashimoto, T. Kaneko, and J. Noaki (JLQCD Collaboration), Phys. Rev. D **92**, 111501 (2015).
[22] M. Tomii, G. Cossu, B. Fahy, H. Fukaya, S. Hashimoto, T. Kaneko, and J. Noaki (JLQCD Collaboration), Phys. Rev. D **94**, 054504 (2016).
[23] G. Martinelli, G. C. Rossi, C. T. Sachrajda, S. R. Sharpe, M. Talevi, and M. Testa, Phys. Lett. B **411**, 141 (1997).
[24] V. Gimenez, L. Giusti, S. Guerriero, V. Lubicz, G. Martinelli, S. Petrarca, J. Reyes, B. Taglienti, and E. Trevigne, Phys. Lett. B **598**, 227 (2004).
[25] K. Cichy, K. Jansen, and P. Korcyl, Nucl. Phys. **B865**, 268 (2012).
[26] K. G. Chetyrkin and A. Maier, Nucl. Phys. **B844**, 266 (2011).
[27] C. Becchi, S. Narison, E. de Rafael, and F. J. Yndurain, Z. Phys. C **8**, 335 (1981).
[28] R. Barate *et al.* (ALEPH Collaboration), Z. Phys. C **76**, 15 (1997).
[29] R. Barate *et al.* (ALEPH Collaboration), Eur. Phys. J. C **4**, 409 (1998).
[30] S. Schael *et al.* (ALEPH Collaboration), Phys. Rep. **421**, 191 (2005).
[31] M. A. Shifman, A. I. Vainshtein, and V. I. Zakharov, Nucl. Phys. **B147**, 385 (1979).
[32] M. Jamin and M. Munz, Z. Phys. C **60**, 569 (1993).
[33] M. Luscher and P. Weisz, Commun. Math. Phys. **97**, 59 (1985); **98**, 433(E) (1985).
[34] C. Morningstar and M. J. Peardon, Phys. Rev. D **69**, 054501 (2004).
[35] M. Luscher, J. High Energy Phys. 08 (2010) 071; 03 (2014) 92.
[36] S. Borsanyi *et al.*, J. High Energy Phys. 09 (2012) 010.
[37] G. Cossu, J. Noaki, S. Hashimoto, T. Kaneko, H. Fukaya, P. A. Boyle, and J. Doi, *Proc. Sci.*, LATTICE2013 (2014) [arXiv:1311.0084].
[38] G. P. Lepage and P. B. Mackenzie, Phys. Rev. D **48**, 2250 (1993).
[39] S. Narison and V. I. Zakharov, Phys. Lett. B **522**, 266 (2001).
[40] S. Aoki *et al.*, Eur. Phys. J. C **77**, 112 (2017).
[41] V. A. Novikov, M. A. Shifman, A. I. Vainshtein, and V. I. Zakharov, Nucl. Phys. **B191**, 301 (1981).